Döring A, Kreis R. Magnetic resonance spectroscopy extended by oscillating diffusion gradients: Cell-specific anomalous diffusion as a probe for tissue microstructure in human brain. Neuroimage. 2019;202:116075.

Magnetic Resonance Spectroscopy Extended by Oscillating Diffusion Gradients:

Cell-Specific Anomalous Diffusion as a Probe for Tissue Microstructure in Human Brain

André Döring[1,2] and Roland Kreis[1]

[1]*Depts. Radiology and Biomedical Research, University of Bern, Bern, Switzerland*

[2]*Graduate School for Cellular and Biomedical Sciences, University of Bern, Bern, Switzerland*

Word count excluding abstract, figure captions and references: 5316

Running Head: *Cell-Specific Anomalous Diffusion as a Probe for Tissue Microstructure in Human Brain*

Corresponding author:

Prof. Dr. sc. nat. Roland Kreis,

AMSM, University Bern,

Erlachstrasse 9a,

CH-3012 Bern, Switzerland

Tel: +41-31-632 8174

Email: roland.kreis@insel.ch

Döring A, Kreis R. Magnetic resonance spectroscopy extended by oscillating diffusion gradients: Cell-specific anomalous diffusion as a probe for tissue microstructure in human brain. Neuroimage. 2019;202:116075.

Abstract

Purpose

To demonstrate that oscillating gradient spin-echo sequences can be combined with diffusion-weighted magnetic resonance spectroscopy even on clinical MR systems to study human brain at short diffusion times to provide apparent diffusion coefficients (ADCs) sensitive to a narrower cellular length scale than pulsed gradient spin-echo sequences at long diffusion time.

Methods

Measurements were performed on a 3T MR system using a semiLaser sequence with diffusion-weighting realized by oscillating and pulsed gradient modules, encoding diffusion times <10 ms and >50 ms, respectively. Metabolite-cycling was included to measure metabolites and water simultaneously. The sequence was tested in a phantom and in a parieto-occipital cerebral region of interest with mixed gray/white matter content of 6 subjects. The water reference was used for phase, frequency, and eddy-current correction as well as motion compensation. ADCs were estimated by 1D sequential and 2D simultaneous fitting.

Results

Measurements in the phantom established that both sequences yield equal ADCs, independent of diffusion time, as expected for free diffusion. In contrast, on average over multiple metabolites in vivo metabolite diffusion was found to be 1.9 times faster at short (8.3 ms) than at long (155 ms) diffusion times. The difference in ADC was found to be statistically significant for the creatines, cholines, N-acetylaspartate, N-acetylaspartylglutamate, myo-inositol, scyllo-inositol, glutamate, glutamine and taurine. The water ADC was measured to be 1.3 times larger at short than at long diffusion time.

Conclusion

It is demonstrated that application of oscillating gradients in diffusion-weighted MRS is feasible on clinical MR systems to establish the dependence of ADCs on diffusion times in humans. The initial results largely confirm earlier reports for mice' and rats' brain at short and long diffusion times. ADCs representing diffusion at short and ultra-short diffusion times are of interest to probe cellular or subcellular changes in disease. The presented methodology may thus open the door for investigation of pathophysiological changes in cell-specific microcellular structures in human cohorts.

Keywords

anomalous diffusion; metabolites; molecular crowding; glia, neurons

1. Introduction

Diffusion-weighted magnetic resonance spectroscopy (DW-MRS[1]) provides information on metabolite diffusion (Nicolay et al., 2001)(Ronen and Valette, 2015)(Cao and Wu, 2017)(Palombo et al., 2017b). Unlike water, metabolites probe intracellular space only and are partially specific to neuronal (e.g. Glu, NAA) or glial (e.g. Ins, Cho) cells(Choi et al., 2007). Hence, metabolite-specific diffusion is a tailored probe for cellular tissue microstructure.

Depending on diffusion time (TD), apparent diffusion coefficients (ADCs) are affected by different dimensions and mechanisms of cellular barriers(Valette et al., 2018). Pulsed gradient spin-echo (PGSE) sequences, commonly used, measure at long TD (>50 ms) where ADCs represent diffusion mostly along tissue fibers(Kroenke et al., 2004)(Najac et al., 2016). Use of oscillating gradient spin-echo (OGSE) sequences sensitive to short TD (<10 ms) promises ADCs more specific to cellular and subcellular properties (e.g. tissue diameter, size, tortuosity) (Marchadour et al., 2012)(Ligneul et al., 2017)(Valette et al., 2018). Thus, one can separate DW-MRS techniques according to the targeted TDs.

At *long TD* present research is mostly concerned with high b-values and directional diffusion encoding. High b-value ($b > 10.000 s/mm^2$) measurements are used to probe deviations from the monoexponential free diffusion decay (Ingo et al., 2018). As recently presented by Palombo et al. even complex structures like neurons or astrocytes can be derived(Palombo et al., 2017a). Another technique aims at directional diffusion (using double diffusion encoding (DDE) (Koch and Finsterbusch, 2008)), where, it was shown that metabolite diffusion can provide characteristic diameters for neurons and astrocytes(Shemesh et al., 2017).

At *short TD* the maximum diffusion-weighting that can be reached is limited. This (together with the faster diffusion constants at short TD) limits explorations at high b values. However, the anomalous diffusion behavior, where the ADC depends on TD, directly encodes tissue specific structural information (Palombo et al., 2016)(Palombo et al., 2018)(Valette et al., 2018). The detailed dependence of ADCs over several orders of TDs is influenced by a multitude of effects (e.g. active transport, tissue specific viscosity, molecular crowding, intracellular tortuosity and barriers (Marchadour et al., 2012)), which is far from trivial to be modeled. However, it has recently been presented for mouse and macaque brain that simulations of anomalous diffusion can be used to draw conclusions on the underlying neuronal and astrocytic structures (Palombo et al., 2019).

A combination of both approaches is required to confirm tissue structure models. Measurements at long TD are most useful to estimate cellular branching and long-range structures, while measurements at short TD are needed to determine system parameters (e.g. cellular viscosity, macromolecular crowding, etc.) and short-range tortuosity.

Up to now the anomalous diffusion behavior in human brain at very short TDs has only been investigated by diffusion-weighted-imaging of water (DWI) and the results have been inconsistent, where anomalous diffusion has been reported by some (Baron and Beaulieu, 2014)(Reynaud et al., 2016) but not by others (Le Bihan et al., 1993)(Clark et al., 2001). The discrepancy may be related to the type of diffusion encoding where cosine-like OGSE appears to be more suited to probe the very short diffusion time regime (Van et al., 2014). However, due to its non-cellular specificity, exchange between compartments, and its fast diffusivity, water is not the ideal agent to probe cell-specific microstructure (Pyatigorskaya et al., 2014).

[1] *for a list of abbreviations, see last page of manuscript*

In contrast, the anomalous diffusion of metabolites promises to provide cell-specific structural information. However, only long TDs have been accessible in DW-MRS for human applications. The present work aims to demonstrate that oscillating gradients can be combined with DW-MRS also on clinical MR systems to study human brain at fairly short TDs to provide metabolite ADCs that are sensitive to a different cellular length scale than with pulsed diffusion-weighting. Initial results obtained when establishing the method in vivo confirm the expected strong dependence of ADCs of metabolites on diffusion time.

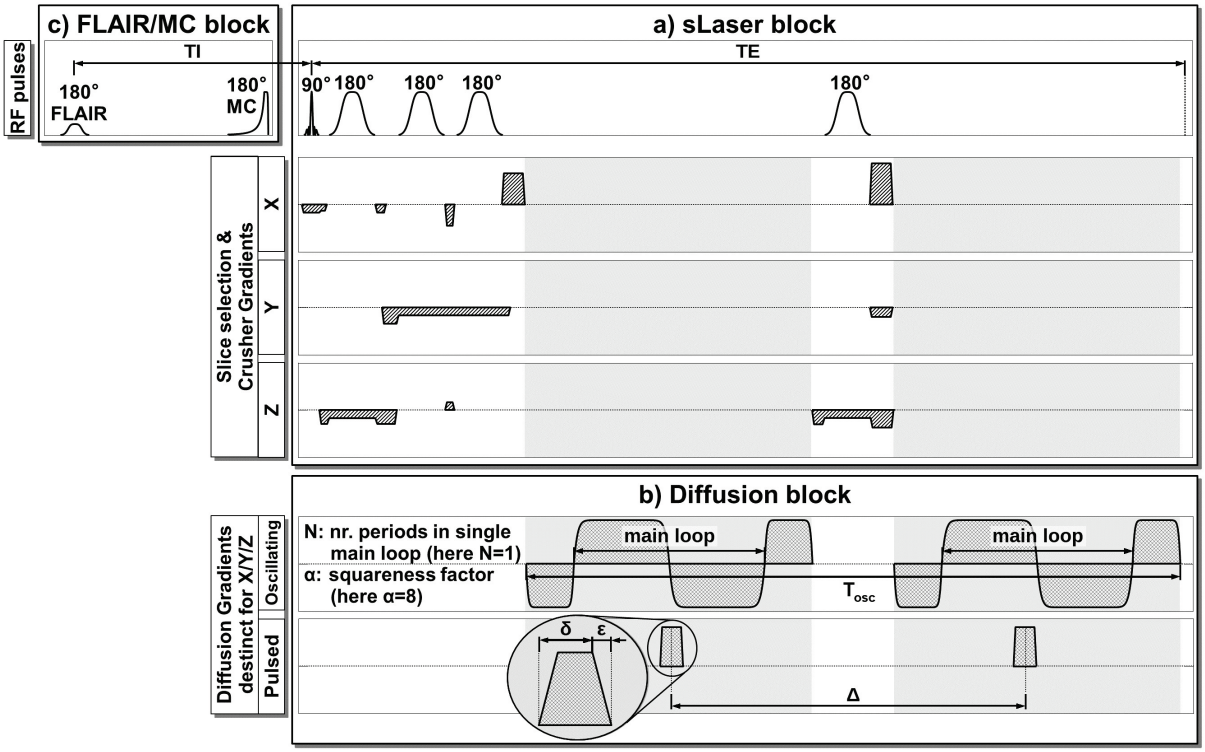

Fig. 1: *Sequence diagram. The semiLaser sequence a) was extended by a diffusion block b) with optional oscillating and pulsed gradients, to measure at short (<10ms) and long (>50ms) diffusion times. Metabolite cycling and FLAIR CSF suppression was placed before localization in block c). The simultaneously acquired inherent water reference was applied for frequency, phase, eddy-current correction and motion-compensation.*

2. Material and methods

2.1. Data acquisition and sequence design

Measurements were performed on a 3T Siemens (Prisma, Siemens, Erlangen, Germany) scanner using a 20-channel head-coil with inherent phase-correction for summation of signals from different coil elements. A semiLaser (Öz and Tkáč, 2011) localization sequence (cf. Fig. 1) was implemented and extended to include diffusion-weighting by OGSE (Gross and Kosfeld, 1969)(Does et al., 2003) and PGSE (Stejskal and Tanner, 1965) elements, sensitive to TDs <10 ms and >50 ms, respectively. The diffusion gradients were placed symmetrically before and after the last 180° refocusing pulse. For PGSE, the gradient pulses were trapezoidal with 200 ms ramptime (ε) and 30.7 mT/m maximal gradient strength in each direction (G_{max}) equal for in vivo and in vitro use, and 158.5/110.0 ms gradient spacing (Δ) and 11.5/8.9 ms gradient duration (δ) for in vivo/in vitro application. For OGSE, stretched cosine diffusion gradient waveforms were used as suggested by Ligneul and Valette (2017), where a stretching exponent α serves to control the increase in effective gradient area to counteract limited diffusion-weighting for simple cosine gradients. In both cases, the diffusion direction was chosen along the space diagonal by applying identical diffusion gradient amplitudes on all three axes (minimizing the gradient amplitude and thus induced

motion and eddy-currents for each single direction). The effective TD for PGSE is a well-defined value and can be directly derived from the diffusion gradient geometry depicted in Fig. 1:

$$TD_{eff}^{PGSE} = \Delta - \delta/3 \quad (1)$$

In case of OGSE, the effective TD is a superposition of a spectrum of single TDs and derived from the diffusion frequency ν_{eff} by(Parsons et al., 2006):

$$TD_{eff}^{OGSE} = \frac{1}{4\nu_{eff}^{OGSE}} \quad (2)$$

Here, the effective TD is not calculated in the Mitra limit as suggested by Novikov and Kiselev (Novikov and Kiselev, 2011) (where 1/4 would be replaced by 9/64) because of the relatively low gradient frequencies accessible on clinical scanners and also for ease of comparison with previous reports in animals. To calculate ν_{eff} the square of the gradient modulation spectrum $|F(\nu)|$ for a cosine-modulated waveform is used for weights on the frequency spectrum, where ($|F(\nu)|$ is the Fourier transform of the idealized diffusion gradient shape $G(t)$ without crusher or slice selecting gradients)(Ligneul and Valette, 2017):

$$\nu_{eff}^{OGSE} = \frac{\int_0^\infty \nu\,|F(\nu)|^2 d\nu}{\int_0^\infty |F(\nu)|^2 d\nu} \quad (3)$$

The diffusion-weighting factor b for OGSE was directly derived from numerical integration of $G(t)$

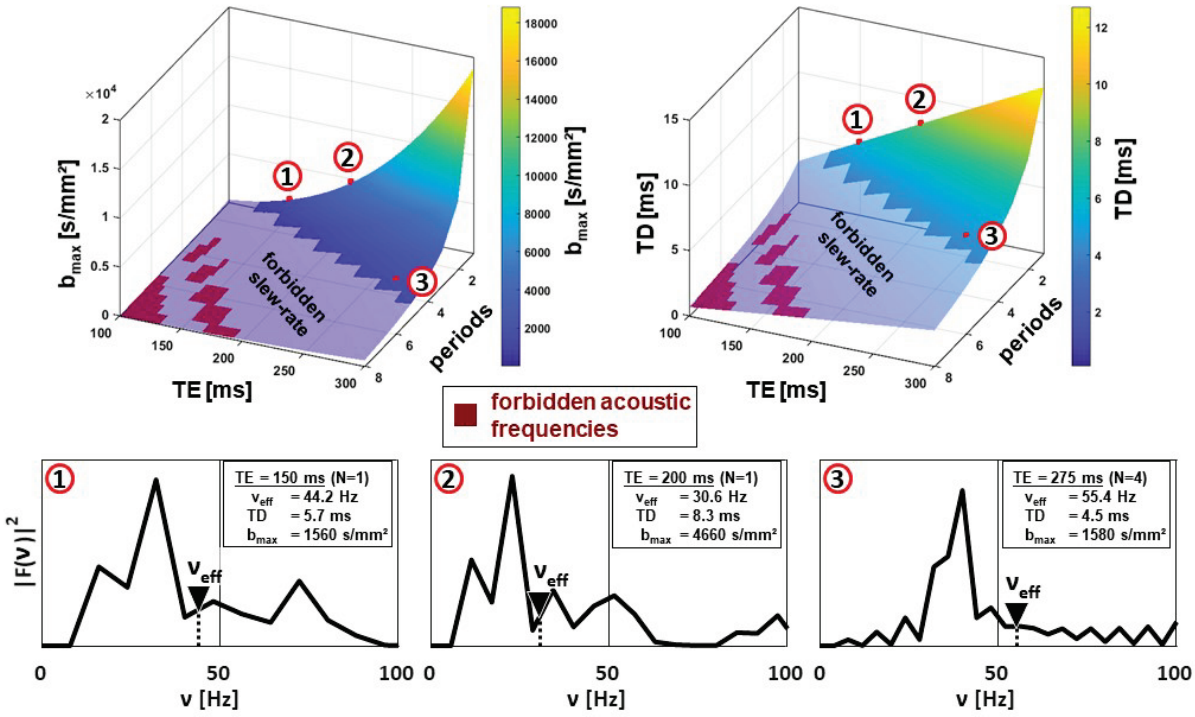

Fig. 2: *Illustration of parameter space accessible with oscillating gradients on a Prisma scanner with maximum gradient strength of 80 mT/m, slew rate of 200 T/m/s and a stretching exponent α of 8. The OGSE parameter space (upper part of the figure) illustrates the dependence of the b-value (left) and of the diffusion time TD (right) on echo time TE and number of periods in the oscillating gradient shape. Three particular points in parameter space are indicated by encircled numbers. They are characterized below by diagrams showing the resulting gradient modulation spectra, where ① was applied in vitro with fast diffusion and ② in vivo with slower diffusion. ③ serves as an example of a possible parametrization with 4 oscillation-periods to reach higher frequencies at the cost of prolonging TE. (not used in this study).*

$$b_{OGSE} = \int_0^{T_{OSC}} dt \left[\gamma \int_0^t G(t')\, dt' \right]^2 \quad (4)$$

whereas for PGSE for reasons of simplicity, the analytical solution in Eq. 5 was used.

$$b_{PGSE} = \gamma^2 G^2 \left[\delta^2 \left(\Delta - \frac{\delta}{3} \right) + \frac{\varepsilon^3}{30} - \frac{\delta \varepsilon^2}{6} \right] \quad (5)$$

It should be noted that this holds when neglecting cross-terms with slice-selection and crusher-gradients. However, a comparison with numerically calculated b-values for our PGSE parameters revealed a deviation <0.1%. The parameter space in terms of b-value and TD as accessible on a clinical scanner ($G_{max}^{total} = 80\ \mathrm{mT/m}$, slew rate of $200\ \mathrm{T/m/s}$) is shown in Fig. 2 as function of echo time (TE) and number of oscillation-periods N. Ranges of forbidden acoustic frequencies were defined as parametrization areas where the ratio of the integral $\int_{\nu_1}^{\nu_2} |F(\nu)|^2 d\nu$ over the forbidden frequency range to the integral $\int_0^{\infty} |F(\nu)|^2 d\nu$ over the whole frequency range exceeds 1%. As example, $|F(\nu)|^2$ is provided for the {TD [ms], b [s/mm²], N} combinations of {5.7, 1560, 1}, {8.3, 4660, 1} and {4.5, 1560, 4} at a=8. For our diffusion measurements, TEs 150 and 200 ms were chosen (N=1). At these TE, PGSE was applied with effective TDs of 107 and 155 ms and maximal b-values of 1716 and 4140 s/mm². For ADC estimation, 8 b-values where recorded, for PGSE as well as OGSE. Background diffusion-weighting arising from crusher and slice-selecting gradients for a typical region of interest (ROI) of 30x30x30 mm³ was estimated to be merely 55 s/mm². Adiabatic metabolite-cycling (MC) (Dreher and Leibfritz, 2005) and water-selective inversion-recovery pulses (Hajnal et al., 2001) were added before localization to acquire water and metabolites simultaneously and to suppress CSF, limiting the water signal to the brain parenchymal space. The CSF suppression was optimized to yield an inversion time (TI) of 1200 ms. First, the semiLaser sequence at TE=150 ms was tested applying PGSE and OGSE in a “braino” phantom (GE medical systems), which is filled with an aqueous solution of the characteristic brain metabolites myo-inositol (mI, 5.0 mM), N-acetylaspartate (NAA, 12.5 mM), glutamate (Glu, 12.5 mM), creatine (Cr, 10.0 mM), lactate (Lac, 5.0 mM), and choline (Cho, 3.0 mM). Subsequently, the sequence was initially tested in vivo (TE = 200 ms; TR = 3000 ms, 57 to 228 seconds scan time per b-value depending on the number of acquisitions) in 6 healthy volunteers (age (45.0±13.1) yrs; range 26-62; 2 women/4 men; scanning of human subjects was endorsed by the local ethics commission; all subjects were screened for potential risk factors for MR investigations and gave their informed consent). Because of the lower signal at higher b-values, the number of acquisitions was increased from 16 to 64 for high b-value scans. The ROI was placed midline in parieto-occipital cortex centered on gray matter (GM), but also containing a considerable proportion of white matter (cf. supplemental Figure S1) . The ROI size was maximized for each volunteer taking care to prevent contamination from subcutaneous fat signal (nominal voxel size: $\mathrm{V_{min}} = 25.2\ \mathrm{mL}$; $\mathrm{V_{max}} = 32.5\ \mathrm{mL}$; $\mathrm{V_{\emptyset}} = (28.6 \pm 2.1)\ \mathrm{mL}$). The flip angle of the excitation pulse was optimized within the ROI using a $\mathrm{B_1}$ map. Shimming was performed using automatic second order “brain-shim” (field-map based shimming method, Prisma, Siemens, Erlangen, Germany) yielding a mean Voigt linewidth of the water signal of $(7.2 \pm 0.5)\ \mathrm{Hz}$ for OGSE and $(7.2 \pm 0.3)\ \mathrm{Hz}$ for PGSE. Probing metabolite diffusion in many other brain regions is expected to be challenged by larger linewidths complicating the quantification of low SNR metabolites with overlapping patterns. Single acquisitions were stored without averaging or preprocessing. The acquired inherent water reference was used not only for phase, frequency and eddy-current correction, but also for compensation of motion artifacts (Döring et al., 2018). No triggering was applied.

2.2. Fitting procedure

The metabolite basis sets were simulated for semiLaser with the versatile simulation, pulses and analysis (VeSPA) toolbox using real pulse shapes, but neglecting the effect of slice-selection gradients (Soher et al., 2017). The in vivo basis set consists of 14 metabolites (Asp: aspartate; Etn: ethanolamine; Gln: glutamine; Glu: glutamate; GSH: glutathione; Lac: lactate; mI: myo-inositol; NAA: N-acetylaspartate; NAAG: N-acetylaspartylglutamate; PE: phosphorylethanolamine; sI: scyllo-inositol; Tau: taurine; tCho: total choline [sum pattern of: glyceryl phosphoryl choline + phosphocholine]; tCr: total creatine [sum pattern of: creatine + phosphocreatine]). Spectra were fitted with FiTAID(Chong et al., 2011) with X^2-minimization in frequency domain restricted to the range between 0 and 4.1 ppm. FiTAID was also used to determine Cramér-Rao lower bounds (CRLBs) for all parameters. Resonances were modeled with Voigt lineshapes.

Except for NAA with 1.1 Hz (corresponding to T_2≈290 ms), all metabolites were modeled with a Lorenz broadening of 2.2 Hz. The field inhomogeneity contribution to the linewidth was included by a common Gaussian broadening. All lines were modeled with equal zero-order phase, frequency offset, and Gaussian broadening at each b-value, all allowed to vary from one b-value to another. Two fitting approaches were considered for ADC estimation. First, sequential fitting was applied to probe monoexponentiality of the signal decay. Second, the whole dataset with all spectra from different b-values were simultaneously fitted imposing a monoexponential signal decay for the diffusion direction together with a spectral linear-combination-model (Adalid et al., 2017). While the latter approach directly yields metabolite ADCs, the former estimates the metabolite areas at each b-value. The corresponding ADCs were estimated by modeling the diffusion decay in MatLab (MathWorks) by weighted fitting, where the inverse CRLBs of the areas where applied as weights. The confidence intervals for the ADCs were calculated using the function *nlparci* in MatLab (based on Jacobian matrix and fitting residuals).

The function describing the Gaussian diffusion (GD) model is the monoexponential decay:

$$A(b, ADC) = A_0 e^{-b\ ADC} \tag{6}$$

where b is the b-value, $A(b)$ the peak area of a specific metabolite at a specific b-value and A_0 the metabolite area without diffusion-weighting. In contrast to the metabolite signal, the water signal is known to decay non-monoexponentially when using b-values >1500 s/mm². This is referred to as non-Gaussian diffusion (nGD). Compared to metabolites, water diffusion is faster and compartmentalized into intra- and extracellular space with exchange between both pools. The Probability Distribution (PD) approach developed by Yablonskiy et al. (2003) takes this into account by describing water diffusion as diffusion of an ensemble of molecules with differing ADCs. The simplest case is a Gaussian distribution with a center value ADC_c and a width σ. This PD approach was used to represent the anomalous diffusion behavior detected for water in vivo when using sequential fitting. The decay function is given by:

$$A(b, ADC, \sigma) = A_0 \frac{1 + \mathrm{erf}\left(\frac{ADC}{\sigma\sqrt{2}} - \frac{b\sigma}{\sqrt{2}}\right)}{1 + \mathrm{erf}\left(\frac{ADC}{\sigma\sqrt{2}}\right)} e^{-b\ ADC + \frac{1}{2}b^2\sigma^2} \tag{7}$$

with $\mathrm{erf}(x)$ the error function of x (Yablonskiy et al., 2003). For σ equal to zero, the PD is a delta distribution and the model coincides with the monoexponential Gaussian diffusion with a single ADC.

Due to good SNR all phantom measurements were sequentially fitted for water and metabolite ADC estimation. The in vivo data were first fitted sequentially in a single subject to probe deviation from monoexponential signal decay for metabolite and water, respectively. For the whole cohort, metabolite ADCs were then fitted simultaneously imposing a monoexponential decay model, while the water ADCs required sequential fitting due to non-monoexponential decay.

All code and data can be made available upon request for non-commercial use except for imaging data that may allow identification of human subjects or methods restricted by confidentiality agreements.

3. Results

3.1. Sequence validation in phantoms

Fig. 3 shows water and metabolite spectra acquired simultaneously by MC in the phantom by PGSE and OGSE, respectively. The b-values were adjusted to be similar for both methods. Visual inspection of spectra shown in Figs. 3A & 3D reveal an almost identical signal attenuation for PGSE and OGSE. Indeed, the signal attenuations of the areas derived from sequential fitting for PGSE and OGSE essentially coincide (Figs. 3B & 3D). To quantify ADCs numerically, the GD model was used for fitting the signal decay of water and metabolites. This yielded almost identical ADCs for PGSE and OGSE, i.e. ADCs that are independent of TD as expected for free diffusion in an aqueous solution (Figs. 3C & 3D). Applying the nGD model instead to fit the water signal decay yields ADCs that are indistinguishable within the error estimates (PGSE: $\mathrm{ADC_C} = (2.15 \pm 0.01) \cdot 10^{-3}\ \mathrm{mm^2/s}$, $\sigma = (0.15 \pm 0.2) \cdot 10^{-3}\ \mathrm{mm^2/s}$; OGSE: $\mathrm{ADC_C} = (2.13 \pm 0.01) \cdot 10^{-3}\ \mathrm{mm^2/s}$, $\sigma = (0.08 \pm 0.10) \cdot 10^{-3}\ \mathrm{mm^2/s}$). To address the possibility of biased ADCs due to different measurement parameterization in vivo, the phantom measurement was repeated for the in vivo conditions with TE=200 ms. The resulting ADCs presented in the supplemental materials in Fig. S2 agree well with the measurements done at TE=150 ms and do

Fig. 3: *Results from sequence validation in a phantom with comparison of PGSE and OGSE scans (signal decays and ADCs derived by sequential fitting in MatLab). Metabolite spectra acquired in a phantom at three different b-values are presented in A) (5 Hz Gaussian apodization for display). The estimated signal decay of the metabolites shown in B) is monoexponential for OGSE and PGSE with identical ADCs as presented in C). The same holds for the simultaneously acquired water spectra, with signal decay and ADCs presented in D).*

not indicate a measurement parameter induced ADC bias.

3.2. In vivo application in human parieto-occipital cortex

The accessible and applicable parameter space of OGSE is limited by the available gradient strength, the metabolite diffusivity and relaxation times, and physiological and hardware safety restrictions (cf. Fig. 2). Given the slower diffusion constants in vivo compared to in vitro, a tradeoff had to be taken to reach an adequate b-value (4660 s/mm²). This included a somewhat prolonged TD (8.3 ms vs. 5.7 ms) and longer TE (200 ms vs. 150 ms).

Fig. 4A shows three diffusion-weighted spectra as examples for acquisitions with PGSE and OGSE in a single subject. A slower signal attenuation in case of PGSE is evident from visual inspection of the spectra. Fig. 4B presents a detailed analysis of the attenuation behavior obtained with sequential fitting. Inspecting the decay of signal areas with increasing diffusion-weighting for the six high concentration metabolites NAA, tCr, tCho, mI, sI and Glu indicates that PGSE does not show motion induced bias to lower intensity at high b-values. Similarly, superficial visual analysis of the OGSE data gives a similar impression. Taking all b-values into account for ADC estimation then yielded a more than 4-fold averaged ADC value for NAA, tCr and tCho (for the cohort data) when moving from long TD (PGSE) to short TD (OGSE), which is clearly much larger than expected from theory and animal data (Najac et al., 2016)(Valette et al., 2018). However, scrutinizing the signal decay for OGSE, one will realize that the area decay is not truly

Fig. 4: *DW spectra and resulting ADCs illustrating results for a scan in a single human subject (signal decays and ADCs derived by sequential fitting in MatLab). The signal attenuation as directly evident from spectra is presented in A) for 3 b-values. It shows generally faster decay for OGSE than PGSE. The signal decays for metabolites plotted in B) obey a monoexponential function for PGSE for the full b-value range, while for OGSE a linear decay model was also fitted for the whole b-value range (dashed red line), but turned out to be inaccurate and an extra signal decay for b values > 1800 s/mm² can be detected upon close inspection – in particular when taking the linear decay model based on the first b-values (solid red line) as a guide. Resulting ADCs for the major metabolites (based on the full b-value range for PGSE and for the restricted b-value range for OGSE) are presented in C). They are consistently higher for OGSE than PGSE (error bars representing the 95%*

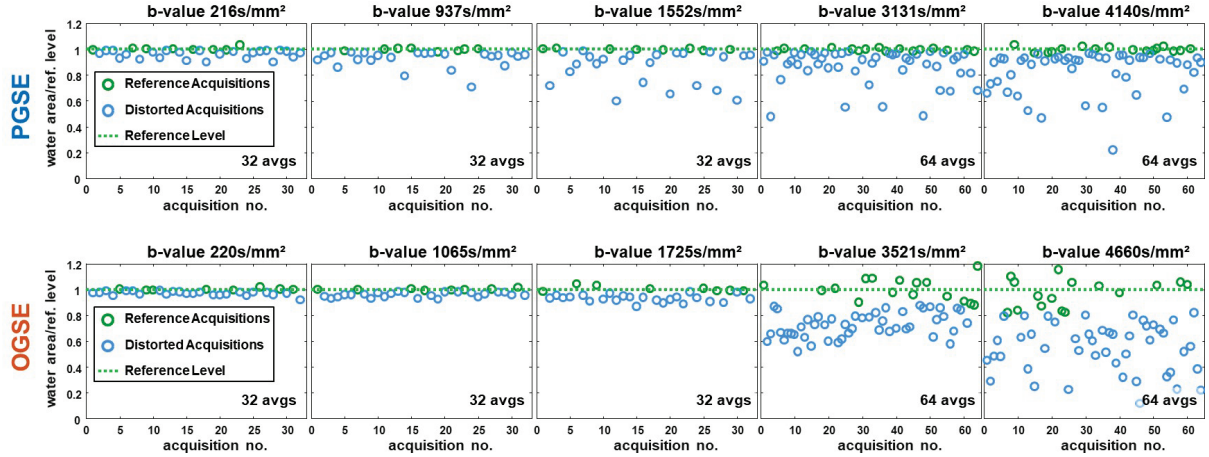

Fig. 5: Illustration of the limits of the motion-compensation scheme for use with oscillating gradients. *Water signal areas (○) normalized to the reference level (dotted green line defined by the median of the upper quartile of water signal areas) for PGSE (upper row) and OGSE (lower row) are shown for five b-values for the same subject as in Fig. 4. The plateau that is visible for all b-values for PGSE and for b<1800 s/mm² for OGSE indicates acquisitions that are not affected by motion; while a reduced area below this plateau indicates scans with compromised by motion. For b-values above 1800 s/mm² no plateau is visible in this and all other subjects for OGSE, which means that virtually all acquisitions in that gradient amplitude range are affected by motion. This prevents signal rescaling to a motion uncompromised reference level for those acquisitions.*

linear in these plots, but rather shows some additional signal loss for b>1800s/mm², most likely due to uncompensated motion in spite of the water-signal-based motion-compensation scheme (Döring et al., 2018).

To investigate this additional signal loss, the water signal areas for all acquisitions in each of five b-value acquisitions were analyzed for all subjects and are plotted in Fig. 5 as illustration for one. A plateau for the maximum signal is clearly visible at all b-values for PGSE, but only for b<1800s/mm² for OGSE. This indicates that for OGSE and high b-values, we cannot assume that the top quartile of all scans (green data in Fig. 5) is unaffected by motion and hence the motion-compensation scheme (based on such an unbiased reference level) will not compensate fully for the motion-induced signal loss. The fitting range for ADC estimation for OGSE was therefore constrained to the five lowest b-values, where the motion-related signal loss can be reliably corrected by the motion-compensation scheme. For PGSE this was not necessary.

For the retained data and within the error bounds, all metabolites showed a monoexponential signal decay. In contrast, the attenuation of the water signal is not monoexponential. To ensure comparability of the water ADC's distributions in the nGD model, both PGSE and OGSE data were constrained to b<1800 s/mm². The signal attenuation and fitting results are presented in Fig. 6A for the same subject as in Fig. 4. It shows clearly a stronger signal decay for OGSE than PGSE. The derived probability distributions for the water ADCs in this single case are illustrated in Fig. 6B with ADC_c for PGSE about 17% below the one for OGSE, while the width of the population is wider in case of PGSE.

The cohort data are presented in Figs. 7 & 8. The metabolite ADCs derived from 2D simultaneous fitting are summarized in Fig. 7 demonstrating that the single result shown in Fig. 4 is typical for the cohort. A paired t-test yields that diffusion is significantly and substantially faster for 5 metabolites for OGSE compared to PGSE. Most significant effects were found for NAA, mI, tCho, tCr and Glu. The metabolite diffusion is found to be 1.9 times faster on average with OGSE at short TD (8.3 ms) than with PGSE at long TD (155 ms).

The cohort water data as estimated with the nGD model is presented in Fig. 8 where the blue area entails the signal decay representing mean and confidence intervals for the short TD and the red area the cohort data for the long TD. As seen in Fig. 8, ADC_c was found to be substantially (1.4 times) higher for OGSE than PGSE ($p<0.05$) with less pronounced deviation from monoexponentiality. The derived mean ADC_cs (±SD) are $(8.1 \pm 1.8) \cdot 10^{-4}\ \mathrm{mm^2/s}$ for PGSE and $(11.1 \pm 1.1) \cdot 10^{-4}\ \mathrm{mm^2/s}$ for OGSE. The mean PD widths (±SD) came out to be 1.3 times smaller for OGSE ($(6.7 \pm 1.9) \cdot 10^{-4}\ \mathrm{mm^2/s}$) than for PGSE ($(8.6 \pm 4.2) \cdot 10^{-4}\ \mathrm{mm^2/s}$). The standard deviation over the cohort indicated by the filled area is comparable for OGSE and PGSE.

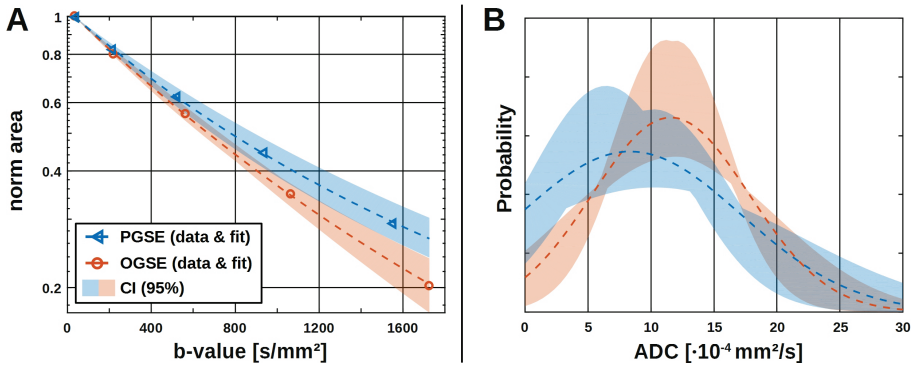

Fig. 6: *The water signal together with the fitting results from the probability distribution (PD) model for the same subject as presented in Fig. 4 constraint to b<1800 s/mm² (sequential fitting in MatLab). The signal decay in A) is not monoexponential for neither OGSE nor PGSE, respectively. For PGSE, the deviation from monoexponentiality is stronger, but well reproduced in both cases by PD model fitting. The resulting PDs in B) reveal a lower ADC_c and higher σ for PGSE (ADC_c: $8.3 \cdot 10^{-4}$ mm²/s; σ: $8.8 \cdot 10^{-4}$ mm²/s) than OGSE (ADC_c: $11.6 \cdot 10^{-4}$*

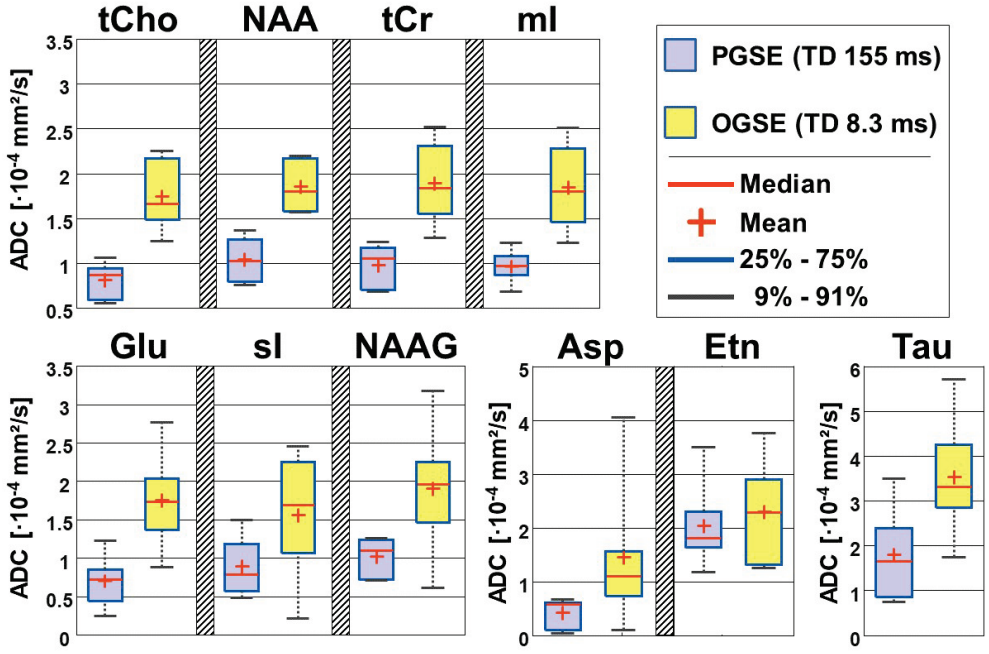

Fig. 7: *Cohort results for metabolite ADC values obtained at two vastly different diffusion times from 6 healthy volunteers (simultaneous fitting in FiTAID). The ADCs reflect a significantly faster diffusion for NAA, tCho, mI ($p<0.01$) and also tCr, Glu ($p<0.05$) at short diffusion times. Individual volunteer data are supplied in Fig. S3 and tabulated as numerical values in Table S1 in the supplemental files. For OGSE, the b-value range was constrained to a maximum b-value of 1725 s/mm² to ensure a reliable water reference for motion compensation as discussed in the text.*

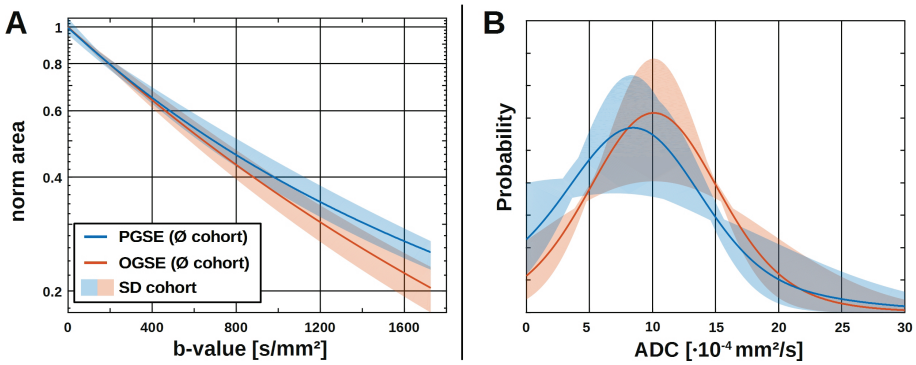

Fig. 8: *The results from nGD model fitting of water for the cohort are presented for the signal decay in A) and for the PD function in B) constrained to b_{max}<1800s/mm² (sequential fitting in MatLab). Colored lines represent the mean parameter values and the colored regions indicate the confidence interval (± 2 SD range for both parameters) over the cohort. The decay with OGSE is found to be faster and more non-monoexponential than with PGSE. The estimated mean ADC for OGSE is significantly (p<0.05) higher than that for PGSE. In contrast, the mean width σ of the PD for OGSE is lower than that for PGSE.*

4. Discussion

The presented work shows that the anomalous diffusion behavior expected for water and metabolites in human brain tissue can readily be observed with the proposed single voxel MRS sequence equipped with pulsed and oscillating diffusion gradient modules on a clinical MR system at 3T. Furthermore, the proposed sequence has the advantage that water and metabolite diffusion can be measured simultaneously. The achievable diffusion times, given the hardware and physiologic limits, have been summarized in Fig. 2 and roughly confirm the limits put forward in Jones et al. (2018). The extent of the diffusion time dependence of metabolite ADCs as found in this study suggests that gradient strengths available in clinical MR systems may offer observation of diffusion regimes that are more sensitive to short-range tissue microstructure.

The DW semiLaser sequence has been validated in vitro, where measurements yielded equal and monoexponential signal decay both at short (<10 ms) and long (>100 ms) diffusion times as determined with oscillating and pulsed gradients for water and metabolites. This is in line with expectation for free diffusing particles in an aqueous solution and demonstrates that the sequence does not introduce an experimental bias when switching from one diffusion module to the other, which is important when interpreting the in vivo results. Comparison with literature reveals similar metabolite ADCs for NAA, Cr and Cho (Ellegood et al., 2005). Also the water ADC of $2.16 \cdot 10^{-3}\ \mathrm{mm^2/s}$ (monoexponential model, at 20°C) is consistent with the free diffusivity found by similar, but also other measurement techniques (Easteal et al., 1989)(Ligneul and Valette, 2017).

Diffusion of water and metabolites are governed by quite distinct conditions. On one hand, water diffuses considerably faster and thus probes a much larger space than metabolites in the same time. On the other hand, the water signal is an overlay of intra- and extracellular components influenced by diffusion in both subspaces, all cell types in terms of intracellular space and also exchange between most compartments. Metabolites in contrast are mostly of intracellular origin, are in parts exclusive for certain cell types and remain within cells over the relevant times. We thus discuss results for water and metabolite diffusion separately.

4.1. Diffusion of water

In agreement with literature, water diffusion was found to be non-monoexponential also with this MRS acquisition method that localizes a large volume—much bigger than ordinary pixel size in MRI—when extending the b-value range to moderately large values (>1500 s/mm²). Investigation of the details of the non-mono-exponential nature of the signal decay

is beyond the aim of this contribution. However, to still be able to investigate the differences between the diffusion decay found at quite short vs. long diffusion times we have chosen a simple Gaussian population distribution model to represent the data. For both diffusion time regimes, this model appears fairly well suited to describe the signal decay as presented in Fig. 6 for a single subject. The CI for the ADC_c's is below 25% for PGSE and OGSE in single subject measurements, while the CI for the width of the distribution is notably higher (50% for OGSE and 80% for PGSE), which may point at the limits of the applicability of the model or to intrinsic measurement inaccuracies (e.g. different ROI composition) or artifacts. Simulations of metabolite diffusion in brain cell structures confirm a Gaussian like PD for an ideal undistorted measurement (Palombo et al., 2016). In reality, unaccounted-for motion would bias ADCs to larger values skewing the PD. Also, if the FLAIR module would not perform sufficiently well, residual signal contributions from CSF, which are expected to be intrinsically large with this big ROI and long echo time, would also contribute additional faster components to the population distribution. However, it is not expected that these effects would strongly bias the differences found for the two diffusion time regimes in the case of water and even less so for the case of metabolites.

The cohort data presented in Fig. 8A show clearly that the water signal decays faster at short than long TD, reflected in a 31% higher ADC at short TD ($p<0.05$). This agrees well with values reported in literature(Portnoy et al., 2013)'(Baron and Beaulieu, 2014). It should be noted, that ADC values reported from mice or rats are below those from humans, while the relative difference in ADC value between long and short TD is similar (Portnoy et al., 2013)(Palombo et al., 2016). This may hint at different cellular length scales or crowding densities (due to macromolecules, organelles) (Oberheim et al., 2009)(Herculano-Houzel, 2014)(Palombo et al., 2016). The observed signal decay, faster for OGSE than PGSE with non-monoexponential tendency in both cases, is reproduced in simulations and experimental findings (Portnoy et al., 2013)(Pyatigorskaya et al., 2014)(Palombo et al., 2019).

In a previous study from our group (Döring et al., 2018) with a similar technique (MC, FLAIR, water referenced motion compensation) and a similarly long range diffusion time (164 ms) but recorded at shorter TE (37 ms), the ADC for water ($(7.7 \pm 0.4) \cdot 10^{-4}\ \mathrm{mm^2/s}$) was found to be 5% below the value determined with PGSE in this study. The difference may partly be explained by different evaluation and b-value range, but possibly partially also by signal contributions at short TE from myelin water with much lower ADC (MacKay et al., 1994)(Harkins and Does, 2016).

4.2. Diffusion of metabolites

The current study successfully yielded metabolite ADCs for human cerebral tissue at long diffusion times that can readily be compared to literature but it yielded also values at short diffusion times where the only comparable data in the literature is from rodent brain. Fig. 9 provides a comparison of major metabolite ADCs found in the literature distinguishing between ADC values from different species.

At long TD (PGSE) the currently reported values compare fairly well with previously reported data, which includes those found by our group in an previous study (Döring et al., 2018) with a stimulated echo technique at short TE (deviations of 4% and 12% for the averaged differences in median and mean ADCs[2]). Compared to ADCs reported by other groups for human GM at similar TD, the presently found ADC values agree well, with some coefficients slightly lower than those from others (Najac et al., 2016)(Ingo et al., 2018). It should be noted however that the currently evaluated ROI includes a substantial fraction of WM as well, which would bias these values to higher ADCs than with pure GM at long TD (Kan et al., 2012).

[2] *Ethanolamine and aspartate excluded because of large variance at long TE in this study.*

Fig. 9: *Comparison of some of the metabolite ADCs found in this study with previously published data split according to species and plotted as a function of the square root of the diffusion time. It is evident that the presently determined data compares well with literature for the long diffusion times, confirms the apparently faster diffusion at short TD previously established for rodent brain. Comparison data was taken from Refs (Pfeuffer et al., 2000)(Ellegood et al., 2005)(Valette et al., 2007)(Kan et al., 2012)(Marchadour et al., 2012)(Najac et al., 2014)(Ercan et al., 2015)(Palombo et al., 2016)*(Najac et al., 2016)*(Ligneul and Valette, 2017)(Deelchand et al., 2018)(Döring et al., 2018)(Ingo et al., 2018).*

There is data from mice and rats that covers the whole range of diffusion times from values that are much longer than what is reported here for PGSE to values that are much shorter than the times reached in our OGSE scans. However, for humans the shortest TD so far was obtained with PRESS in a PGSE experiment with a TD of 25 ms, 3 times longer than for the presently reported data and thus not well suited for comparison since the ADCs are expected to increase substantially only when approaching TDs <10 ms. In terms of rodent studies at very short TD, there are three reported studies (Marchadour et al., 2012)(Ligneul and Valette, 2017)(Ligneul et al., 2017) to compare with. The earliest work was with rats (Marchadour et al., 2012), where ADCs were reported for NAA, tCho and tCr for 6 TDs between 1 and 13 ms. The best agreement with our human values is found for longer TD at 12.9 ms in the rat study (of note, in a later report the authors suspected the ADCs to have been biased somewhat towards too high values because of motion effects). The best study to compare to seems to be the one by Ligneul and Valette (2017) performed in mice, where motion was compensated for using a macromolecule signal as internal reference. ADCs for NAA, tCr, tCho, Tau and mI were reported for 5 different oscillation frequencies (35 Hz to 252 Hz) and, thus, TDs. At the lowest frequency of 35 Hz (4 Hz above what was used in this study) the resulting ADCs were 15% smaller than our present findings (when neglecting Tau which shows the largest discrepancy the difference is merely 10%). Moreover, it can be expected that ADCs estimated under non-narcotized conditions would be even lower (Valette et al., 2007) and hence this effect might increase the difference somewhat. Thus, from this comparison and from inspection of the overall TD dependence plotted in Fig. 9 it seems that the ADC values reported presently for very short TD in human brain appear to be a little higher than expected, but reasons for these slightly larger metabolite ADCs at moderately low TD are manifold. Besides plain measurement inaccuracies, differences in white/gray matter composition (Ingo et al., 2018), species differences (substantially larger (by cross section) neurons (Herculano-Houzel, 2014) and protoplasmic astrocytes (Oberheim et al., 2009) have been reported for human compared to rodent brain), remaining effects of motion (potentially mechanical tissue resonances at the applied OGSE frequencies (Ligneul and Valette, 2017)) or different measurement conditions (e.g. echo time) can easily lead to systematic differences of 10% for a multi-site multi-species comparison.

Döring A, Kreis R. Magnetic resonance spectroscopy extended by oscillating diffusion gradients: Cell-specific anomalous diffusion as a probe for tissue microstructure in human brain. Neuroimage. 2019;202:116075.

4.3. Limitations

A couple of limitations of this study should be mentioned.

1) As discussed earlier, the b-value range that provided reliable data was constrained to below 1800 s/mm² for OGSE because of substantial residual motion effects that affected the water signal in OGSE in most acquisitions such that the proposed motion-compensation algorithm based on an undistorted water signal did not perform adequately. It should be investigated whether somewhat altered stimulation frequencies or different brain regions would suffer less from this effect. Alternatively, investigations at shorter echo time (possible only with scanners offering much higher diffusion gradient amplitudes (Jones et al., 2018)) could make use of macromolecular signals for an alternative approach for motion compensation (Ligneul and Valette, 2017).

2) The investigated ROI was fairly large to optimize signal to noise in this initial study, which lead to a mixture of white and gray matter content. Subsequent investigation should be carried out to look at more homogeneous white and gray matter areas.

3) A single diffusion direction has been probed in the current study with emphasis on comparison of sequences rather than exploration of directional dependence, which may well be non-negligible, given a fairly large white matter contribution to the ROI. It will be of interest to investigate directional dependence in areas of white matter with homogeneous fiber direction.

4) The number of subjects investigated was small and results especially for the less prominent metabolites should be corroborated in larger cohorts – e.g. the fast diffusion constants for taurine or the very slow diffusion for aspartate at long TD.

5. Conclusion

A semiLaser diffusion sequence with PGSE and OGSE was developed and successfully tested in vitro and in vivo. It is demonstrated in human brain that application of OGSE reveals significantly increased metabolite ADCs compared to PGSE, indicating an increased sensitivity to diffusion on the cellular and subcellular level at short TD. We hope that subsequent studies will confirm a higher sensitivity for pathophysiological ADC changes at short TD.

Funding

This work is supported by the Swiss National Science Foundation (SNSF #320030-156952 and #320030-175984).

Döring A, Kreis R. Magnetic resonance spectroscopy extended by oscillating diffusion gradients: Cell-specific anomalous diffusion as a probe for tissue microstructure in human brain. Neuroimage. 2019;202:116075.

References

Adalid, V., Döring, A., Kyathanahally, S.P., Bolliger, C.S., Boesch, C., Kreis, R., 2017. Fitting interrelated datasets: metabolite diffusion and general lineshapes. Magn. Reson. Mater. Physics, Biol. Med. 30, 429–448. https://doi.org/10.1007/s10334-017-0618-z

Baron, C.A., Beaulieu, C., 2014. Oscillating gradient spin-echo (OGSE) diffusion tensor imaging of the human brain. Magn. Reson. Med. 72, 726–736. https://doi.org/10.1002/mrm.24987

Cao, P., Wu, E.X., 2017. In vivo diffusion MRS investigation of non-water molecules in biological tissues. NMR Biomed. 30, e3481. https://doi.org/10.1002/nbm.3481

Choi, J.-K., Dedeoglu, A., Jenkins, B.G., 2007. Application of MRS to mouse models of neurodegenerative illness. NMR Biomed. 20, 216–237. https://doi.org/10.1002/nbm.1145

Chong, D.G.Q., Kreis, R., Bolliger, C.S., Boesch, C., Slotboom, J., 2011. Two-dimensional linear-combination model fitting of magnetic resonance spectra to define the macromolecule baseline using FiTAID, a Fitting Tool for Arrays of Interrelated Datasets. MAGMA 24, 147–164. https://doi.org/10.1007/s10334-011-0246-y

Clark, C.A., Hedehus, M., Moseley, M.E., 2001. Diffusion time dependence of the apparent diffusion tensor in healthy human brain and white matter disease. Magn. Reson. Med. 45, 1126–1129. https://doi.org/10.1002/mrm.1149

Deelchand, D.K., Auerbach, E.J., Marjańska, M., 2018. Apparent diffusion coefficients of the five major metabolites measured in the human brain in vivo at 3T. Magn. Reson. Med. 79, 2896–2901. https://doi.org/10.1002/mrm.26969

Does, M.D., Parsons, E.C., Gore, J.C., 2003. Oscillating gradient measurements of water diffusion in normal and globally ischemic rat brain. Magn. Reson. Med. 49, 206–215. https://doi.org/10.1002/mrm.10385

Döring, A., Adalid, V., Boesch, C., Kreis, R., 2018. Diffusion-weighted magnetic resonance spectroscopy boosted by simultaneously acquired water reference signals. Magn. Reson. Med. 80, 2326–2338. https://doi.org/10.1002/mrm.27222

Dreher, W., Leibfritz, D., 2005. New method for the simultaneous detection of metabolites and water in localized in vivo 1H nuclear magnetic resonance spectroscopy. Magn. Reson. Med. 54, 190–195. https://doi.org/10.1002/mrm.20549

Easteal, A.J., Price, W.E., Woolf, L.A., 1989. Diaphragm cell for high-temperature diffusion measurements. tracer diffusion coefficients for water to 363 K. J. Chem. Soc. Faraday Trans. 1 Phys. Chem. Condens. Phases 85, 1091. https://doi.org/10.1039/f19898501091

Ellegood, J., Hanstock, C.C., Beaulieu, C., 2005. Trace apparent diffusion coefficients of metabolites in human brain using diffusion weighted magnetic resonance spectroscopy. Magn. Reson. Med. 53, 1025–32. https://doi.org/10.1002/mrm.20427

Ercan, A.E., Techawiboonwong, A., Versluis, M.J., Webb, A.G., Ronen, I., 2015. Diffusion-weighted chemical shift imaging of human brain metabolites at 7T. Magn. Reson. Med. 73, 2053–2061. https://doi.org/10.1002/mrm.25346

Gross, B., Kosfeld, R., 1969. Anwendung der Spin-Echo-Methode bei der Messung der Selbstdiffusion. Messtechnik 77, 171–177.

Hajnal, J. V., Oatridge, A., Herlihy, A.H., Bydder, G.M., 2001. Reduction of CSF artifacts on FLAIR images by using adiabatic inversion pulses. Am. J. Neuroradiol. 22, 317–322.

Harkins, K.D., Does, M.D., 2016. Simulations on the influence of myelin water in diffusion-weighted imaging. Phys. Med. Biol. 61, 4729–4745. https://doi.org/10.1088/0031-9155/61/13/4729

Herculano-Houzel, S., 2014. The glia/neuron ratio: How it varies uniformly across brain structures and species and what that means for brain physiology and evolution. Glia 62, 1377–1391. https://doi.org/10.1002/glia.22683

Ingo, C., Brink, W., Ercan, E., Webb, A.G., Ronen, I., 2018. Studying neurons and glia non-invasively via anomalous subdiffusion of intracellular metabolites. Brain Struct. Funct. 223, 3841–3854. https://doi.org/10.1007/s00429-018-

1719-9

Jones, D.K., Alexander, D.C., Bowtell, R., Cercignani, M., Dell'Acqua, F., McHugh, D.J., Miller, K.L., Palombo, M., Parker, G.J.M., Rudrapatna, U.S., Tax, C.M.W., 2018. Microstructural imaging of the human brain with a 'super-scanner': 10 key advantages of ultra-strong gradients for diffusion MRI, NeuroImage. Elsevier Inc. https://doi.org/10.1016/j.neuroimage.2018.05.047

Kan, H.E., Techawiboonwong, A., van Osch, M.J., Versluis, M.J., Deelchand, D.K., Henry, P.G., Marjanska, M., van Buchem, M.A., Webb, A.G., Ronen, I., 2012. Differences in apparent diffusion coefficients of brain metabolites between grey and white matter in the human brain measured at 7 T. Magn. Reson. Med. 67, 1203–1209.

Koch, M.A., Finsterbusch, J., 2008. Compartment size estimation with double wave vector diffusion-weighted imaging. Magn. Reson. Med. 60, 90–101. https://doi.org/10.1002/mrm.21514

Kroenke, C.D., Ackerman, J.J.H., Yablonskiy, D.A., 2004. On the nature of the NAA diffusion attenuated MR signal in the central nervous system. Magn. Reson. Med. 52, 1052–1059. https://doi.org/10.1002/mrm.20260

Le Bihan, D., Turner, R., Douek, P., 1993. Is water diffusion restricted in human brain white matter? An echo-planar NMR imaging study. Neuroreport 4, 887–890.

Ligneul, C., Palombo, M., Flament, J., Valette, J., 2017. Approaching free intracellular diffusion by diffusion-weighted MRS at ultra-short time scales: initial results in the rodent brain using a 1.5 T/m gradient., in: Proc. Intl. Soc. Mag. Reson. Med. p. 1082.

Ligneul, C., Valette, J., 2017. Probing metabolite diffusion at ultra-short time scales in the mouse brain using optimized oscillating gradients and "short"-echo-time diffusion-weighted MRS. NMR Biomed. 30, e3671. https://doi.org/10.1002/nbm.3671

MacKay, A., Whittall, K., Adler, J., Li, D., Paty, D., Graeb, D., 1994. In vivo visualization of myelin water in brain by magnetic resonance. Magn. Reson. Med. 31, 673–677.

Marchadour, C., Brouillet, E., Hantraye, P., Lebon, V., Valette, J., 2012. Anomalous diffusion of brain metabolites evidenced by diffusion-weighted magnetic resonance spectroscopy in vivo. J. Cereb. Blood Flow Metab. 32, 2153–2160. https://doi.org/10.1038/jcbfm.2012.119

Najac, C., Branzoli, F., Ronen, I., Valette, J., 2016. Brain intracellular metabolites are freely diffusing along cell fibers in grey and white matter, as measured by diffusion-weighted MR spectroscopy in the human brain at 7 T. Brain Struct. Funct. 221, 1245–1254. https://doi.org/10.1007/s00429-014-0968-5

Najac, C., Marchadour, C., Guillermier, M., Houitte, D., Slavov, V., Brouillet, E., Hantraye, P., Lebon, V., Valette, J., 2014. Intracellular metabolites in the primate brain are primarily localized in long fibers rather than in cell bodies, as shown by diffusion-weighted magnetic resonance spectroscopy. Neuroimage 90, 374–380. https://doi.org/10.1016/j.neuroimage.2013.12.045

Nicolay, K., Braun, K.P.J., Graaf, R.A. de, Dijkhuizen, R.M., Kruiskamp, M.J., 2001. Diffusion NMR spectroscopy. NMR Biomed. 14, 94–111. https://doi.org/10.1002/nbm.686

Novikov, D.S., Kiselev, V.G., 2011. Surface-to-volume ratio with oscillating gradients. J. Magn. Reson. 210, 141–145. https://doi.org/10.1016/j.jmr.2011.02.011

Oberheim, N.A., Takano, T., Han, X., He, W., Lin, J.H.C., Wang, F., Xu, Q., Wyatt, J.D., Pilcher, W., Ojemann, J.G., Ransom, B.R., Goldman, S.A., Nedergaard, M., 2009. Uniquely hominid features of adult human astrocytes. J. Neurosci. 29, 3276–3287. https://doi.org/10.1523/JNEUROSCI.4707-08.2009

Öz, G., Tkáč, I., 2011. Short-echo, single-shot, full-intensity proton magnetic resonance spectroscopy for neurochemical profiling at 4 T: Validation in the cerebellum and brainstem. Magn. Reson. Med. 65, 901–910. https://doi.org/10.1002/mrm.22708

Palombo, M., Alexander, D.C., Zhang, H., 2019. A generative model of realistic brain cells with application to numerical simulation of the diffusion-weighted MR signal. Neuroimage 188, 391–402. https://doi.org/10.1016/j.neuroimage.2018.12.025

Palombo, M., Ligneul, C., Hernandez-Garzon, E., Valette, J., 2018. Can we detect the effect of spines and leaflets on the diffusion of brain intracellular metabolites? Neuroimage 182, 283–293. https://doi.org/10.1016/j.neuroimage.2017.05.003

Palombo, M., Ligneul, C., Najac, C., Le Douce, J., Flament, J., Escartin, C., Hantraye, P., Brouillet, E., Bonvento, G., Valette, J., 2016. New paradigm to assess brain cell morphology by diffusion-weighted MR spectroscopy in vivo. Proc. Natl. Acad. Sci. 113, 6671–6676. https://doi.org/10.1073/pnas.1504327113

Palombo, M., Ligneul, C., Valette, J., 2017a. Modeling diffusion of intracellular metabolites in the mouse brain up to very high diffusion-weighting: Diffusion in long fibers (almost) accounts for non-monoexponential attenuation. Magn. Reson. Med. 77, 343–350. https://doi.org/10.1002/mrm.26548

Palombo, M., Shemesh, N., Ronen, I., Valette, J., 2017b. Insights into brain microstructure from in vivo DW-MRS. Neuroimage 1–20. https://doi.org/10.1016/j.neuroimage.2017.11.028

Parsons, E.C., Does, M.D., Gore, J.C., 2006. Temporal diffusion spectroscopy: Theory and implementation in restricted systems using oscillating gradients. Magn. Reson. Med. 55, 75–84. https://doi.org/10.1002/mrm.20732

Pfeuffer, J., Tkac, I., Gruetter, R., 2000. Extracellular-intracellular distribution of glucose and lactate in the rat brain assessed noninvasively by diffusion-weighted 1H nuclear magnetic resonance spectroscopy in vivo. J. Cereb. Blood Flow Metab. 20, 736–746.

Portnoy, S., Flint, J.J., Blackband, S.J., Stanisz, G.J., 2013. Oscillating and pulsed gradient diffusion magnetic resonance microscopy over an extended b-value range: Implications for the characterization of tissue microstructure. Magn. Reson. Med. 69, 1131–1145. https://doi.org/10.1002/mrm.24325

Pyatigorskaya, N., Le Bihan, D., Reynaud, O., Ciobanu, L., 2014. Relationship between the diffusion time and the diffusion MRI signal observed at 17.2 tesla in the healthy rat brain cortex. Magn. Reson. Med. 72, 492–500. https://doi.org/10.1002/mrm.24921

Reynaud, O., Winters, K.V., Hoang, D.M., Wadghiri, Y.Z., Novikov, D.S., Kim, S.G., 2016. Surface-to-volume ratio mapping of tumor microstructure using oscillating gradient diffusion weighted imaging. Magn. Reson. Med. 76, 237–247. https://doi.org/10.1002/mrm.25865

Ronen, I., Valette, J., 2015. Diffusion-weighted magnetic resonance spectroscopy, in: EMagRes. John Wiley & Sons, Ltd, Chichester, UK, pp. 733–750. https://doi.org/10.1002/9780470034590.emrstm1471

Shemesh, N., Rosenberg, J.T., Dumez, J.N., Grant, S.C., Frydman, L., 2017. Distinguishing neuronal from astrocytic subcellular microstructures using in vivo double diffusion encoded 1H MRS at 21.1 T. PLoS One 12, 1–19. https://doi.org/10.1371/journal.pone.0185232

Soher, B., Semanchuk, P., Todd, D., Young, K., 2017. Vespa: Versatile Simulation, Pulses and Analysis for MR Spectroscopy [WWW Document]. URL http://scion.duhs.duke.edu/vespa/

Stejskal, E.O., Tanner, J.E., 1965. Spin diffusion measurements: spin echoes in the presence of a time-dependent field gradient. J. Chem. Phys. 42, 288–292. https://doi.org/10.1063/1.1695690

Valette, J., Guillermier, M., Besret, L., Hantraye, P., Bloch, G., Lebon, V., 2007. Isoflurane strongly affects the diffusion of intracellular metabolites, as shown by 1H nuclear magnetic resonance spectroscopy of the monkey brain. J. Cereb. Blood Flow & Metab. 27, 588–596. https://doi.org/10.1038/sj.jcbfm.9600353

Valette, J., Ligneul, C., Marchadour, C., Najac, C., Palombo, M., 2018. Brain metabolite diffusion from ultra-short to ultra-long time scales: What do we learn, where should we go? Front. Neurosci. 12, 1–6.

Döring A, Kreis R. Magnetic resonance spectroscopy extended by oscillating diffusion gradients: Cell-specific anomalous diffusion as a probe for tissue microstructure in human brain. Neuroimage. 2019;202:116075.

https://doi.org/10.3389/fnins.2018.00002

Van, A.T., Holdsworth, S.J., Bammer, R., 2014. In vivo investigation of restricted diffusion in the human brain with optimized oscillating diffusion gradient encoding. Magn. Reson. Med. 71, 83–94. https://doi.org/10.1002/mrm.24632

Yablonskiy, D.A., Bretthorst, G.L., Ackerman, J.J.H., 2003. Statistical model for diffusion attenuated MR signal. Magn. Reson. Med. 50, 664–669. https://doi.org/10.1002/mrm.10578

List of abbreviations

ADC	apparent diffusion coefficients
Asp	aspartate
CI	confidence interval
CSF	cerebrospinal fluid
DDE	double diffusion encoding
Etn	ethanolamine
FiTAID	Fitting Tool for Interrelated Arrays of Datasets
FLAIR	fluid-attenuated inversion recovery
GD	Gaussian diffusion
Gln	glutamine
Glu	glutamate
GM	gray matter
GSH	glutathione
Lac	lactate
LASER	localization by adiabatic selective refocusing
MC	metabolite cycling
mI	myo-inositol
NAA	N-acetylaspartate
NAAG	N-acetylaspartylglutamate
nGD	non-Gaussian diffusion
OGSE	oscillating gradient spin-echo
PD	probability distribution
PE	phosphorylethanolamine
PGSE	pulsed gradient spin-echo
PRESS	point-resolved spectroscopy
ROI	region of interest
SD	standard deviation
sI	scyllo-inositol
Tau	taurine
tCho	total choline
tCr	total creatine
TD	diffusion time
TE	echo time
TI	inversion time
TR	repetition time
VeSPA	versatile simulation, pulses and analysis
WM	white matter

Figure S1

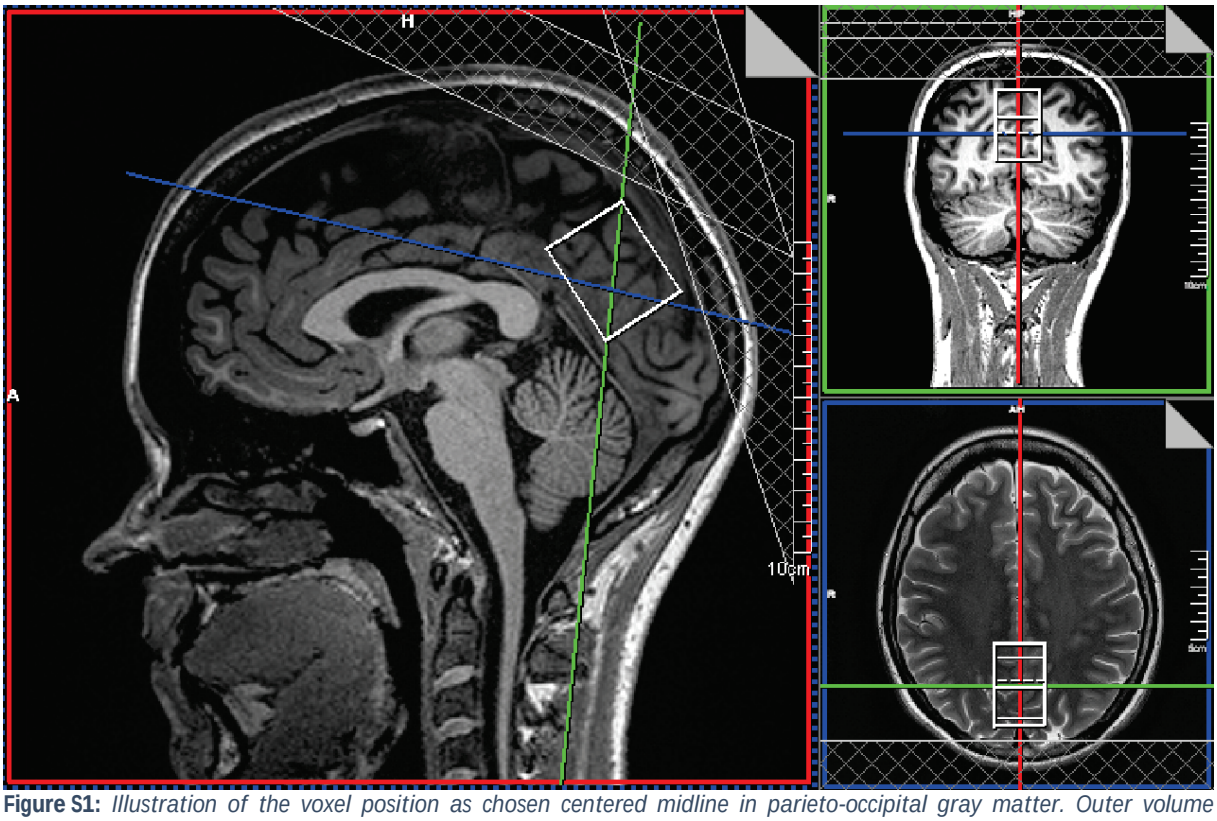

Figure S1: *Illustration of the voxel position as chosen centered midline in parieto-occipital gray matter. Outer volume suppression bands were placed to suppress lipid contamination from subcutaneous fat signal.*

Figure S2

Figure S2 presents the metabolite ADCs obtained from the same phantom as presented in Fig. 3, but with equal parametrization as applied for the in vivo measurements (TE=200 ms). The obtained ADCs agree well between short TD (8.3 ms) with oscillating gradient spin-echo (OGSE) and long TD (155 ms) with pulsed gradient spin-echo (PGSE) diffusion encoding. This experiment shows that motion induced by table vibrations at this parametrization is of neglectable effect for PGSE and OGSE in a phantom. However, due to faster diffusion compared to the in vivo situation, the maximum b-value was restricted to 1700 s/mm². Therefore, the maximum gradient amplitudes were below those applied for the in vivo situation. However, even in vivo we had to restrict the b-value range to b<1800s/mm².

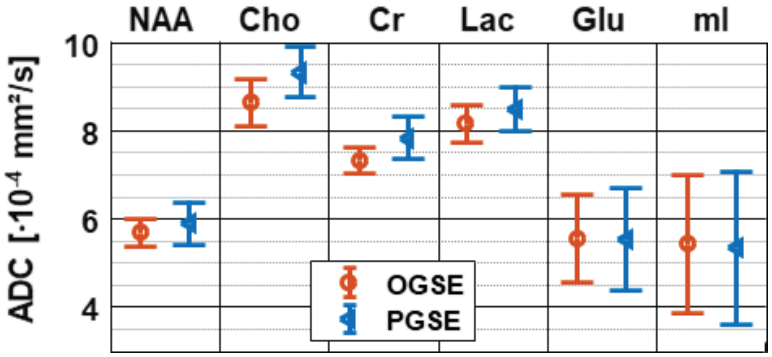

Figure S2: *Metabolite ADCs obtained in the phantom as presented in Fig. 3, but with equal echo time (TE) and diffusion gradient shapes as applied for the in vivo measurements (TE=200ms; b_{max}=1725s/mm²; TD=8.3ms [f=30.6Hz]; sequential fitting in MatLab).*

Figure S3

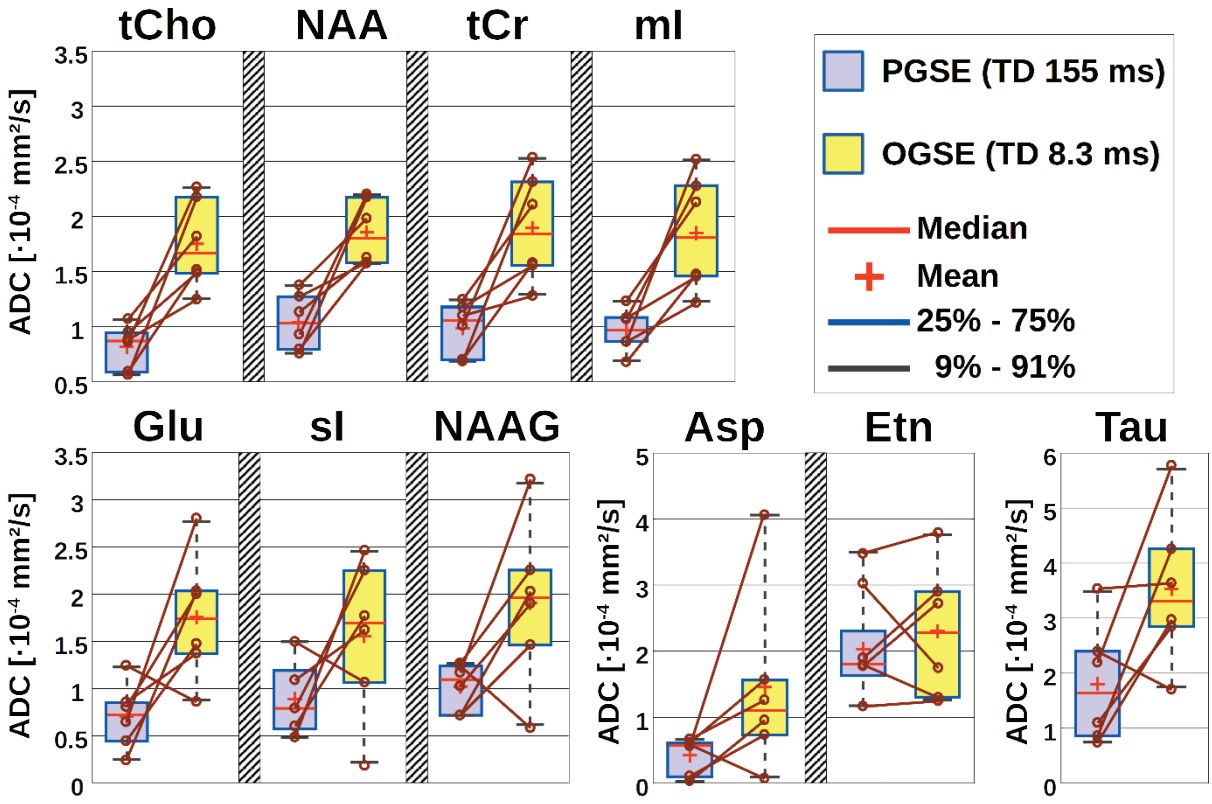

Figure S3: *Box plot of metabolite ADCs for the cohort of healthy subjects as presented in Fig. 6, but here with indication of correspondance of individual volunteers ADCs between short (PGSE) and long (OGSE) diffusion times (simultaneous fitting in FiTAID).*

For one volunteer no ADC was found for sI in the case of PGSE. The first row summarizes metabolites where ADCs increase for all volunteers.

Table S1

Table S1: Cohort summary for *metabolite ADC values as presented graphically in Fig. 7 and Fig. S3 with their means, medians and standard deviations (SD) and in addition the median CRLB fit error estimates (simultaneous fitting in FiTAID).*

metab	Mean ADC		Median ADC		SD ADC		Median CRLBs	
	PGSE	OGSE	PGSE	OGSE	PGSE	OGSE	PGSE	OGSE
tCho	0.8	1.7	0.9	1.7	0.2	0.4	0.03	0.04
NAA	1.0	1.9	1.1	1.8	0.2	0.3	0.02	0.03
tCr	0.9	1.9	1.1	1.8	0.2	0.5	0.03	0.03
mI	1.0	1.8	1.0	1.8	0.2	0.5	0.08	0.10
Glu	0.7	1.8	0.7	1.7	0.3	0.7	0.10	0.11
sI	0.9	1.6	0.8	1.7	0.4	0.8	0.18	0.30
NAAG	1.0	1.9	1.1	2.0	0.2	0.9	0.11	0.12
Asp	0.4	1.5	0.6	1.1	0.3	1.4	0.18	0.20
Etn	2.0	2.3	1.8	2.3	0.8	1.0	0.25	0.29
Tau	1.8	3.5	1.6	3.3	1.0	1.4	0.35	0.54

$\cdot 10^{-4}$ mm²/s